MMOD-induced structural changes of hydroxylase in soluble methane monooxygenase

Hanseong Kim[1], Sojin An[1], Yeo Reum Park[2], Hara Jang[2], Sang Ho Park[1], Seung Jae Lee[2,*] & Uhn-Soo Cho[1,*]

[1]*Department of Biological Chemistry, University of Michigan, Ann Arbor, MI 48109, USA*

[2]*Department of Chemistry, Chonbuk National University, Jeonju 54896, Republic of Korea*

Summary

Soluble methane monooxygenase in methanotrophs converts methane to methanol under ambient conditions[1-3]. The maximum catalytic activity of hydroxylase (MMOH) is achieved via interplay of its regulatory protein (MMOB) and reductase[4-6]. An additional auxiliary protein, MMOD, is believed to function as an inhibitor of the catalytic activity of MMOH; however, the mechanism of its action remains unknown[7,8]. Herein, we report the crystal structure of MMOH–MMOD complex from *Methylosinus sporium* strain 5 (2.6 Å), which illustrates that two molecules of MMOD associate symmetrically with the canyon region of MMOH in a manner similar to MMOB, indicating that MMOD competes with MMOB for MMOH recognition. Further, MMOD binding disrupts the geometry of the di-iron centre and opens the substrate access channel. Notably, the electron density of 1,6-hexanediol at the substrate access channel mimics products of sMMO in hydrocarbon oxidation. The crystal structure of MMOH–MMOD unravels the inhibitory mechanism by which MMOD suppresses the MMOH catalytic activity, and reveals how hydrocarbon substrates/products access to the di-iron centre.

24 Methanotrophs have an ability to use methane as their sole energy and carbon source[9,10]. The
25 critical enzymes participating in this conversion process are particulate methane monooxygenase
26 and soluble methane monooxygenase (sMMO)[11-13]. In particular, the sMMO enzyme, which
27 belongs to the bacterial multicomponent monooxygenase superfamily, carries out the following
28 reaction:

29 $$CH_4 + O_2 + 2H^+ + 2e^- \rightarrow CH_3OH + H_2O \quad (1)$$

30 The effectiveness of catalysis by sMMO is known to be linked to the interplay of three sMMO
31 components: MMO hydroxylase (MMOH), MMO reductase (MMOR) and MMO regulatory
32 protein (MMOB)[4-6]. MMOH, which performs the chemical conversion of methane to methanol,
33 is a homodimer of three subunits (α, β and γ), with a glutamate- and histidine-coordinated non-
34 heme di-iron centre at each α-subunit[1,2]. MMOR shuttles electrons from nicotinamide adenine
35 dinucleotide (NADH) to the di-iron centre in MMOH[14]. MMOB is a regulatory component that
36 alters reduction potentials at the di-iron centre and helps the substrate to access the active
37 site[15,16]. It has been shown that there is another auxiliary protein in the sMMO operon, called
38 MMOD (*orfY*), which is proposed to inhibit the catalytic activity of MMOH[7,8] and the 'copper-
39 switch' in methanotrophs[17,18]. However, the molecular mechanism by which MMOD performs
40 its function towards MMOH remains undetermined.

41 The crystal structure of MMOH and the NMR structures of MMOB and two MMOR domains
42 have been determined, and their potential roles in the catalytic reaction have been proposed[19-23].
43 However, the absence of structures of MMOH in complex with its auxiliary proteins has made it
44 difficult to fully elucidate the chemistry of sMMO in substrate oxidation. We reported previously
45 the crystal structure of the MMOH–MMOB complex at 2.9 Å resolution[15]. Structural studies of

46 MMOH–MMOB have addressed key questions about how MMOB modulates the geometry of
47 the di-iron centre and the substrate access channel. However, to fully understand the enzymatic
48 mechanism utilised for the conversion of methane to methanol by MMOH, additional structural
49 information is required. In particular, structural information regarding how auxiliary proteins
50 such as MMOR and MMOD influence the catalytic activity of MMOH upon binding, as well as
51 the ingress and egress pathways of substrates and products in sMMO is currently missing.

52 We began to elucidate the molecular mechanism by which MMOD influences the catalytic
53 activity of MMOH by determining the crystal structure of the MMOH–MMOD complex from *M.*
54 *sporium* strain 5 at 2.6 Å resolution (Fig. 1a). The initial electron density map of the MMOH–
55 MMOD complex was calculated by molecular replacement using *Methylosinus trichosporium*
56 OB3b MMOH as the search model (PDB ID: 1MHY)[20]. *M. trichosporium* OB3b MMOH and *M.*
57 *sporium* strain 5 MMOH enzymes are highly homologous, sharing primary sequence identity of
58 97% (α-subunit), 88% (β-subunit) and 87% (γ-subunit) (Extended Data Fig. 1a,b). The crystal
59 structure of the MMOH–MMOD complex reveals that two copies of MMOD interact
60 symmetrically with MMOH via its canyon region (Fig. 1a,b). The conserved core region of
61 MMOD (residues 8–71) has a well-ordered structure and harbours a ββββα-fold architecture with
62 four N-terminal anti-parallel β-strands and a long C-terminal α-helix (Fig. 1c and Extended Data
63 Fig. 1c). Residues 1–11 and 76–111 of MMOD, which are less conserved among other strains,
64 are disordered in the crystal structure.

65 MMOD binds to helices E, F and H of the MMOH α-subunit (MMOHα) through a β4 and an α1
66 helix (Fig. 2a,b). The side chain of Gln45 and the peptide backbone of residues 48 and 49 in
67 MMOD β4 form hydrogen bond interactions with Thr241, Glu240 (helix F) and Asn214 (helix
68 E) of MMOHα (Fig. 2b). Side chains and the backbone of MMOD Leu50 and Ser51 (MMOD

69 loop) participate in hydrophobic and hydrogen bond interactions with Trp317 and Asp312 (helix
70 H) of MMOHα (Fig. 2c). In the long α-helix of MMOD, residues including Ser54, His61, Ser64,
71 His65, Arg68, Gln69 (hydrogen bond) and Val62 (hydrophobic) interact with Asp312 (helix H),
72 Val218, Ser225 (helix E), Glu230 and Leu237 (helix F) of MMOHα (Fig. 2d).

73 The crystal structure of the MMOH–MMOB complex demonstrated that MMOB also associates
74 with the canyon region of MMOH generated by two MMOH α-subunits (Extended Data Fig.
75 2a)[15]. Structural comparison between the MMOH–MMOB and MMOH–MMOD complexes
76 indicates strongly that MMOD and MMOB compete for binding at the canyon region of MMOH,
77 thereby inhibiting the catalytic activity of MMOH (Extended Data Fig. 2b). Indeed, the catalytic
78 activity of MMOH is reduced in the presence of increasing amounts of MMOD, as reported
79 earlier in *M. capsulatus* (Bath) sMMO counterparts (Fig. 2e)[7,8]. The affinity measurements of
80 MMOB and MMOD towards MMOH using fluorescence quenching of MMOH demonstrated
81 comparable dissociation constants (Fig. 2f and Extended Data Table 2). The truncated MMODs
82 (residues 1–74, 12–111 and 12–74) displayed slightly, but not significantly, reduced binding
83 affinities, suggesting that the conserved core region of MMOD observed in the crystal structure
84 is essential for MMOH recognition (Extended Data Table 2).

85 In order to illustrate the influence of MMOD binding on the overall architecture of MMOH, as
86 well as the geometry of the di-iron centre, the structures of MMOH and the MMOH–MMOD
87 complex were compared. This comparison revealed a major conformational change in the N-
88 terminus of the MMOH β-subunit (MMOHβ-NT) (Fig. 3a). Specifically, MMOHβ-NT becomes
89 disordered upon MMOD binding (Extended Data Fig. 3a). A clash between the N-terminal helix
90 of MMOHβ and the C-terminal long helix of MMOD results in MMOHβ-NT being pushed
91 away, thereby dissociating it from MMOHα (Fig. 3b and Extended Data Fig. 3a). Since

92 MMOHβ-NT functions as a 'latch' to hold the MMOHα (Extended Data Fig. 4a), the disorder of
93 MMOHβ-NT (residues 1–56 of the β-subunit) initiates conformational changes in MMOHα,
94 particularly helices A, B and C (Extended Data Fig. 3b, c). The di-iron centre at MMOHα is
95 coordinated by four glutamates and two histidines provided by the four-helix bundle composed
96 of helices B, C, E and F (Fig. 3c). The conformational changes in helices B and C, induced by
97 MMOHβ-NT disorganisation, induce in turn geometric changes in the di-iron centre and
98 rearrangement of the di-iron coordination (Fig. 3c,d). Particularly, His147 (helix C) displays a
99 significant conformational change that dissociates it from Fe1 coordination and allows one water
100 molecule to place in between Fe1 and His147 (Fig. 3d). The glutamate residues that coordinate
101 the two iron atoms also rearrange their coordination upon MMOD association. For example,
102 upon MMOD binding, both Glu114 and Glu144 recognise Fe1 in a bidentate/chelating manner
103 through the carboxylate shift owing to the movement of helix B and C, respectively (Fig. 3c, d
104 and Extended Data Fig. 3b, c). In addition, Glu243 interacts with Fe2 in a bidentate manner. To
105 the best of our knowledge, the dissociation of His147 and bidentate coordination of Glu114
106 unravelled in the MMOH–MMOD complex have not been observed in previous MMOH-related
107 structures (Fig. 3d and Extended Data Fig. 4). Notably, the discoordination of His147 from the
108 di-iron active site (Fe1–His147 Nδ1 distance within two protomers: 5.27 Å / 4.98 Å) may further
109 inhibit the catalytic activity of MMOH.

110 The extent of structural reorganisation in the di-iron centre caused by MMOD binding is
111 comparable to that caused by MMOB binding. It has been shown that the binding of MMOB
112 induces conformational changes at helices E and F, which subsequently push Glu243 (helix F)
113 into the di-iron centre (Fig. 3c and Extended Data Fig. 5a, b). Consequently, this change
114 squeezes the two Fe atoms of the centre between Glu243 (helix F) and Glu144 (helix C), thereby

115 leading to a change in reduction potential at the di-iron centre (Extended Data Fig. 5b)[16,24].
116 While MMOB binding induces the rotation of helices E and F, the MMOD binding disorganises
117 MMOHβ-NT, thereby allowing the translational movement of helices B and C (Extended Data
118 Figs. 3c and 5c). As a consequence, MMOB binding changes the reduction potential and MMOD
119 binding inhibits the catalytic activity of MMOH.

120 Upon building the model structure of the MMOH–MMOD complex, we detected unidentified
121 electron density near the di-iron centre. When we placed 1,6-hexanediol (one of the compounds
122 used in the crystallisation) over this unknown electron density, a good fit was obtained after
123 refinement (Fig. 4a). sMMO is known to oxidise a variety of hydrocarbons, including alkanes
124 from methane to octane[5]. The presence of 1,6-hexanediol near the di-iron centre can be explained
125 by opening of the channel, mediated by the side-chain rearrangement of Leu110 and Phe188,
126 both of which function together as a gate for substrate and product passage to the active site (Fig.
127 4b)[15,19,25,26]. A similar type of channel opening has also been observed in the MMOH–MMOB
128 complex (Extended Data Fig. 6a, b)[15]. This observation indicates that the channel opening in the
129 MMOH–MMOD complex is also driven by the MMOD association. Examination of other
130 previously reported product-soaked crystal structures of MMOH showed that products or product
131 analogues are mostly trapped at cavities as a result of the channel closure mediated by Leu110
132 and Phe188 (Extended Data Fig. 6c). By contrast, 1,6-hexanediol is able to reach the di-iron
133 centre via the substrate access channel in the MMOH–MMOD complex because the binding of
134 MMOD opens the continuous channel (Fig. 4a). The disorganisation of MMOHβ-NT after the
135 association of MMOH with MMOD, followed by structural relaxation of MMOHα generates
136 additional tunnels inside of MMOH (Extended Data Fig. 7). The current MMOH–MMOD
137 structure also supports the hypothesis that both substrate ingress and product egress take place

138 through the substrate access channel, and not through the pore located near the active site, at
139 least for hydrocarbon chain substrates such as hexane[5,26].

140 The crystal structures of the MMOH–MMOB and MMOH–MMOD complexes indicate that
141 MMOB and MMOD associate competitively with the canyon region of MMOH. The results of
142 hydrogen-deuterium exchange mass spectrometry analysis and computational docking studies in
143 the MMOH–MMOR complex also corroborate the model in which MMOR associates with the
144 canyon region of MMOH[27]. This strongly suggests that all three auxiliary proteins of sMMO
145 modulate the catalytic activity of MMOH through their competitive association at the canyon
146 region (Fig. 4c).

147 The MMOH–MMOD structure determined in this work indicates that MMOD functions as an
148 inhibitor for MMOH by competing with MMOB for MMOH association, as well as by
149 disrupting the productive geometry of the di-iron centre (Fig. 4c). The potential of MMOD to
150 function as a 'copper-switch', in addition to its inhibitory role, needs to be investigated
151 further[17,18]. Taken together, the crystal structure of the MMOH–MMOD complex and the
152 MMOH–MMOB structure determined previously demonstrate the mechanism by which
153 auxiliary proteins modulate the catalytic activity of MMO hydroxylase, which involves inducing
154 differentiated conformational changes in MMOH as well as at the di-iron centre.

155

156 **References**

157

158 1 Merkx, M. *et al.* Dioxygen activation and methane hydroxylation by soluble methane
159 monooxygenase: a tale of two irons and three proteins. *Angew. Chem. Int. Ed.* **40**, 2782–
160 2807 (2001).

161 2 Wallar, B. J. & Lipscomb, J. D. Dioxygen activation by enzymes containing binuclear
162 non-heme iron clusters. *Chem. Rev.* **96**, 2625–2658 (1996).

163 3 Leahy, J. G., Batchelor, P. J. & Morcomb, S. M. Evolution of the soluble diiron
164 monooxygenases. *FEMS Microbiol. Rev.* **27**, 449–479 (2003).

165 4 Tinberg, C. E. & Lippard, S. J. Revisiting the mechanism of dioxygen activation in
166 soluble methane monooxygenase from M. capsulatus (Bath): evidence for a multi-Step,
167 proton-dependent reaction pathway. *Biochemistry* **48**, 12145–12158 (2009).

168 5 Wang, W., Liang, A. D. & Lippard, S. J. Coupling oxygen consumption with
169 hydrocarbon oxidation in bacterial multicomponent monooxygenases. *Acc. Chem. Res.*
170 **48**, 2632–2639 (2015).

171 6 Gassner, G. T. & Lippard, S. J. Component interactions in the soluble methane
172 monooxygenase system from Methylococcus capsulatus (Bath). *Biochemistry* **38**, 12768–
173 12785 (1999).

174 7 Merkx, M. & Lippard, S. J. Why OrfY? Characterization of MMOD, a long overlooked
175 component of the soluble methane monooxygenase from Methylococcus capsulatus
176 (Bath). *J. Biol. Chem.* **277**, 5858–5865 (2002).

177 8 Sazinsky, M. H., Merkx, M., Cadieux, E., Tang, S. & Lippard, S. J. Preparation and X-
178 ray structures of metal-free, dicobalt and dimanganese forms of soluble methane

179 monooxygenase hydroxylase from Methylococcus capsulatus (Bath). *Biochemistry* **43**,
180 16263–16276 (2004).
181 9 Higgins, I. J., Best, D. J. & Hammond, R. C. New findings in methane-utilizing bacteria
182 highlight their importance in the biosphere and their commercial potential. *Nature* **286**,
183 561–564 (1980).
184 10 Hanson, R. S. & Hanson, T. E. Methanotrophic bacteria. *Microbiol. Rev.* **60**, 439–471
185 (1996).
186 11 Balasubramanian, R. & Rosenzweig, A. C. Structural and mechanistic insights into
187 methane oxidation by particulate methane monooxygenase. *Acc. Chem. Res.* **40**, 573–580
188 (2007).
189 12 Tinberg, C. E. & Lippard, S. J. Dioxygen activation in soluble methane monooxygenase.
190 *Acc. Chem. Res.* **44**, 280–288 (2011).
191 13 Semrau, J. D., DiSpirito, A. A. & Yoon, S. Methanotrophs and copper. *FEMS Microbiol.*
192 *Rev.* **34**, 496–531 (2010).
193 14 Kopp, D. A., Gassner, G. T., Blazyk, J. L. & Lippard, S. J. Electron-transfer reactions of
194 the reductase component of soluble methane monooxygenase from Methylococcus
195 capsulatus (Bath). *Biochemistry* **40**, 14932–14941 (2001).
196 15 Lee, S. J., McCormick, M. S., Lippard, S. J. & Cho, U. S. Control of substrate access to
197 the active site in methane monooxygenase. *Nature* **494**, 380–384 (2013).
198 16 Paulsen, K. E. *et al.* Oxidation-reduction potentials of the methane monooxygenase
199 hydroxylase component from Methylosinus trichosporium OB3b. *Biochemistry* **33**, 713–
200 722 (1994).

201 17 Semrau, J. D. *et al.* Methanobactin and MmoD work in concert to act as the 'copper-
202 switch' in methanotrophs. *Environ. Microbiol.*, 3077–3086 (2013).
203 18 Yan, X., Chu, F., Puri, A. W., Fu, Y. & Lidstrom, M. E. Electroporation-based genetic
204 manipulation in type I methanotrophs. *Appl. Environ. Microbiol.* **82**, 2062–2069 (2016).
205 19 Rosenzweig, A. C., Frederick, C. A., Lippard, S. J. & Nordlund, P. Crystal-structure of a
206 bacterial nonheme iron hydroxylase that catalyzes the biological oxidation of methane.
207 *Nature* **366**, 537–543 (1993).
208 20 Elango, N. *et al.* Crystal structure of the hydroxylase component of methane
209 monooxygenase from Methylosinus trichosporium OB3b. *Protein Sci.* **6**, 556–568
210 (1997).
211 21 Chatwood, L. L., Müller, J., Gross, J. D., Wagner, G. & Lippard, S. J. NMR structure of
212 the flavin domain from soluble methane monooxygenase reductase from Methylococcus
213 capsulatus (Bath). *Biochemistry* **43**, 11983–11991 (2004).
214 22 Müller, J., Lugovskoy, A. A., Wagner, G. & Lippard, S. J. NMR structure of the [2Fe-2S]
215 ferredoxin domain from soluble methane monooxygenase reductase and interaction with
216 its hydroxylase. *Biochemistry* **41**, 42–51 (2002).
217 23 Walters, K. J., Gassner, G. T., Lippard, S. J. & Wagner, G. Structure of the soluble
218 methane monooxygenase regulatory protein B. *Proc. Natl. Acad. Sci. USA* **96**, 7877–
219 7882 (1999).
220 24 Fox, B. G., Liu, Y., Dege, J. E. & Lipscomb, J. D. Complex-formation between the
221 protein-components of methane monooxygenase from methylosinus-trichosporium Ob3b
222 - identification of sites of component interaction. *J. Biol. Chem.* **266**, 540–550 (1991).

223 25 Rosenzweig, A. C. *et al.* Crystal structures of the methane monooxygenase hydroxylase
224 from Methylococcus capsulatus (Bath): implications for substrate gating and component
225 interactions. *Proteins* **29**, 141–152 (1997).
226 26 Sazinsky, M. H. & Lippard, S. J. Product bound structures of the soluble methane
227 monooxygenase hydroxylase from Methylococcus capsulatus (Bath): protein motion in
228 the alpha-subunit. *J. Am. Chem. Soc.* **127**, 5814–5825 (2005).
229 27 Wang, W., Iacob, R. E., Luoh, R. P., Engen, J. R. & Lippard, S. J. Electron transfer
230 control in soluble methane monooxygenase. *J. Am. Chem. Soc.* **136**, 9754–9762 (2014).
231

232 **Methods**

233 ***M. sporium* strain 5 fermentation and purification of MMOH**

234 *M. sporium* strain 5 (ATCC35069) was cultured in nitrate mineral salts (NMS) media (ATCC
235 1306) at 30 °C until OD_{655} reached 8–10 with a methane:air (v/v) ratio of 10–15%[28]. The cells
236 were harvested by centrifugation (11,300 × *g*) for 20 min at 4°C. The cell pellets were suspended
237 in a lysis buffer containing 3-(*N*-morpholino)propanesulfonic acid (MOPS, 25 mM), NaCl (25
238 mM), sodium thioglycolate (8 mM), L-cysteine (2 mM), $(NH_4)_2Fe(SO4)_2 \cdot 6H_2O$ (200 μM),
239 $MgCl_2$ (5 mM), DNase (0.25 μL/mL) and phenylmethane sulfonyl fluoride (PMSF, 0.04 mg/mL)
240 at pH 6.5. The dissolved suspension was sonicated at 4 °C (CV334 model, Sonics), and the
241 lysate was centrifuged at 30,000 × *g* for 45 min at 4 °C. The supernatant was carefully decanted
242 and filtered through a 0.22-μm membrane (EMD Millipore). The filtrate was loaded onto DEAE
243 Sepharose Fast Flow, Superdex 200, and Q Sepharose Fast Flow columns attached to the ATKA
244 Pure 25L FPLC system (GE healthcare) to purify MMOH with >95% purity[4,29]. The purified
245 MMOH was applied to a ferrozine assay to monitor the iron-ferrozine complex (562 nm), and the
246 results revealed 3.9–4.2 Fe/MMOH with R^2 values >0.999[15].

247

248 **Expression and purification of MMOB and MMOR**

249 Both recombinant *mmoB* (MMOB) and *mmoC* (MMOR) in a pET30a(+) plasmid were
250 transformed into *Escherichia coli* BL21(DE3) cells (Novagen) and cultured in LB media
251 containing 50 μg/mL kanamycin at 37 °C. The cultures were induced for 5 h with 1.0-mM
252 isopropyl β-D-1-thiogalactopyranoside (IPTG) before harvesting by centrifugation at 4 °C. The

253 MMOB cell pellets were re-suspended in solution containing phosphate (pH 6.0, 25 mM), NaCl
254 (75 mM), $MgCl_2$ (5 mM). Na_2-EDTA (1 mM), DTT (dithiotheritol, 1 mM), DNase I (0.25
255 μL/mL) and PMSF (0.04 mg/mL). The suspended cells were lysed by sonication at 4 °C. The
256 filtered supernatant was applied to Q Sepharose Fast Flow and Superdex 75 columns to purify
257 MMOB with >95% purity[23,30]. The MMOR cell pellets were re-suspended in solution containing
258 MOPS (pH 6.5, 25 mM), sodium thioglycolate (8 mM), L-cysteine (2 mM), NaCl (25 mM),
259 $(NH_4)_2Fe(SO4)_2 \cdot 6H_2O$ (200 μM), $MgCl_2$ (5 mM), DNase I (1 unit/mL) and PMSF (0.2 mM), and
260 subsequently were sonicated for cell lysis. The lysed cells were centrifuged at 26,000 × *g* at 4 °C
261 for 40 min, filtered (0.22-μm membrane filter) and loaded onto DEAE Sepharose Fast Flow and
262 Q Sepharose columns to purify MMOR[31]. The ferrozine assay confirmed 2.1–2.2 Fe/MMOR
263 with R^2 values >0.999[29].

264

265 **Activity measurement of MMOH**

266 MMOH (1.0 μM), MMOB (2.0 μM) and MMOR (0.5 μM) were added to a 25-mM solution of
267 MOPS (pH 7.5) containing DTT (1 mM) and NaCl (10 mM), and propylene gas was bubbled
268 through the mixture (Hankook Special Gas) for 20 min. Subsequently, the mixture was incubated
269 at 25 °C. Steady-state kinetics were measured using a Cary 60 UV-visible spectrometer by the
270 addition of NADH at 340 nm (ε_{340} = 6,220 $cm^{-1}M^{-1}$). The inhibitory activities of MMOD were
271 measured in the absence or presence of progressively increasing amounts of MMOD. Products
272 were confirmed by gas chromatography (YL 6500GC system) using an Agilent HP-PLOT/Q
273 stationery column (30 m × 0.535 mm × 40.00 μm). Independent experiments were repeated in
274 triplicate to calculate the mean and the standard error of the mean (SEM).

275

276 **MMOD expression and purification**

277 The N-terminal $(His)_{X6}$ and maltose-binding protein (hisMBP)-tagged wild-type *mmoD*
278 (MMOD) was prepared in *Escherichia coli* Rosetta (DE3) with auto-inducible media[32]. Cell
279 pastes were re-suspended in solution containing Tris-HCl (pH 7.5, 30 mM), NaCl (500 mM) and
280 β-mercaptoethanol (5 mM) with protease inhibitor cocktails. After sonication on ice for 3 min,
281 soluble lysate was recovered by centrifugation at 20,000 × g for 30 min and was subsequently
282 applied to a cobalt affinity resin (Takeda). The hisMBP-MMOD proteins were eluted with
283 elution buffer (Tris-HCl = 30 mM, pH 7.5; NaCl = 500 mM; imidazole = 300 mM; β-
284 mercaptoethanol = 5 mM). In order to remove the hisMBP-tag, the elution fraction and Tobacco
285 Etch Virus protease (1:100 ratio) were mixed together in the amylose resin. After overnight
286 incubation at 4 ºC, the flow-through fraction, which contains MMOD, was collected from the
287 amylose resin and loaded onto an HP Q column (GE Healthcare) equilibrated with HEPES (pH
288 7.5, 30 mM), NaCl (100 mM) and DTT (1 mM), and eluted in a 0 to 1000 mM NaCl gradient.
289 Based on the results of SDS-PAGE gel electrophoresis, fractions containing MMOD were
290 pooled. The pooled fractions were concentrated using Amicon (EMD Millipore) and applied to a
291 Superdex200 (10/300) size exclusion chromatography (GE healthcare) column equilibrated in
292 HEPES (pH 7.5, 30 mM), NaCl (100 mM) and TCEP (tris [2-carboxyethyl] phosphine, 1 mM).

293

294 **Crystallisation, data collection and structure determination**

295 Purified MMOH and MMOD (in solution containing HEPES, 30 mM, pH 7.5; NaCl, 100 mM;
296 and TCEP, 1 mM) were mixed in a 1:2 molar ratio and the final concentration was adjusted to 10
297 mg/mL. Plate shape crystals were grown within a week at room temperature using the hanging

298 drop vapour diffusion method with a mixture of 10% (w/v) PEG 8000, 20% (v/v) ethylene
299 glycol, 0.02 M 1,6-hexanediol, 0.02 M 1-butanol, 0.02 M 1,2-propanediol, 0.02 M 2-propanol,
300 0.02 M 1,4-butanediol, 0.02 M 1,3-propanediol, 0.89 M 1,3-butanediol, and 0.1 M
301 MES/imidazole buffer (pH 6.5). After transferring to a cryo-protectant solution containing the
302 precipitant and 35% (w/v) PEG 8000, crystals were flash-frozen in liquid nitrogen. The space
303 group of the crystal was C2 with a = 179.8 Å, b = 125.8 Å, c = 126.4 Å, $\alpha = \gamma = 90^{o}$ and $\beta =$
304 102.9^{o}. The dataset was collected at Advanced Photon Source (APS) on beam line LS-CAT 21
305 ID-G. The 2.6 Å data were processed by HKL2000 (www.hkl-xray.com) and initial phases were
306 calculated by molecular replacement (Phaser)[33] using *Methylosinus trichosporium* OB3b MMOH
307 as the search model (PDB ID: 1MHY)[20]. After molecular replacement, the electron density for
308 MMOD was clearly visible. The MMOD model was subsequently manually built using COOT[34]
309 and the refinement was performed using PHENIX.refine[35]. Iron atoms and ligand restraints were
310 generated using the program PHENIX (PHENIX.metal_coordination and PHENIX.ready_set)
311 and applied during the refinement. No NCS restraints were applied during the refinement. The
312 asymmetric unit contains two copies of each the MMOH α-subunit, β-subunit, γ-subunit and
313 MMOD FL, and the R_{work} and R_{free} values of the final refined model were 17.8 and 22.6,
314 respectively. Residues 1–11 (1–10) and 161–172 (159–171) of the MMOH α-subunit, residues
315 1–56 (1–56) of the MMOH β-subunit, residues 1–4 (1–2) of the MMOH γ-subunit and residues
316 1–11 (1–6) and 76–111 (75–111) of MMOD were disordered and invisible in the final model
317 (Parenthesis indicates residues in the other MMOH protomer). Ramachandran analyses were
318 performed by MolProbity[36] and the results were as follows: 95.4 (favoured), 4.5 (allowed) and
319 0.1% (outlier).

320

321 **Binding affinity measurements**

322 The fluorescence spectra were collected at 25 °C using the PTI QM-400 (HORIBA, CANADA)
323 with monochromators for both excitation and emission[24]. Fluorescence spectra of MMOH (0.32
324 μM of MMOH in 300 μL of 25-mM MOPS and 1-mM DTT [pH 7.0]) were determined using an
325 excitation wavelength of 282 nm. Fluorescence was quantified by integration of fluorescence
326 emission bands with a maximum at 363 nm. The MMOH fluorescence was quenched by titration
327 with MMOB, MMOD and truncated MMODs (residues 1–74, 12–111 and 12–74). These
328 enzymes were titrated to MMOH in the concentration range from 0 to 15 μM. Dissociation
329 constants were determined by fitting the intensity of emission at 363 nm (Origin2018b and
330 Wolfram Mathmatica). Independent experiments were repeated in triplicate to allow the
331 calculation of the average ± SEM.

332

333 **References**

334

335 28 Ali, H., Scanlan, J., Dumont, M. G. & Murrell, J. C. Duplication of the mmoX gene in
336 Methylosinus sporium: cloning, sequencing and mutational analysis. *Microbiology* **152**,
337 2931–2942 (2006).

338 29 Beauvais, L. G. & Lippard, S. J. Reactions of the peroxo intermediate of soluble methane
339 monooxygenase hydroxylase with ethers. *J. Am. Chem. Soc.* **127**, 7370–7378 (2005).

340 30 Brandstetter, H., Whittington, D. A., Lippard, S. J. & Frederick, C. A. Mutational and
341 structural analyses of the regulatory protein B of soluble methane monooxygenase from
342 Methylococcus capsulatus (Bath). *Chem. Biol.* **6**, 441–449 (1999).

343 31 Blazyk, J. L. & Lippard, S. J. Domain engineering of the reductase component of soluble
344 methane monooxygenase from Methylococcus capsulatus (Bath). *J. Biol. Chem.* **279**,
345 5630–5640 (2004).

346 32 Studier, F. W. Protein production by auto-induction in high density shaking cultures.
347 *Protein Expr. Purif.* **41**, 207-234 (2005).

348 33 McCoy, A. J. *et al.* Phaser crystallographic software. *J. Appl. Cryst.* **40**, 658–674 (2007).

349 34 Emsley, P., Lohkamp, B., Scott, W. G. & Cowtan, K. Features and development of Coot.
350 *Acta Crystallogr. D Biol. Crystallogr.* **66**, 486–501 (2010).

351 35 Afonine, P. V. *et al.* Towards automated crystallographic structure refinement with
352 phenix.refine. *Acta Crystallogr. D Biol. Crystallogr.* **68**, 352–367 (2012).

353 36 Chen, V. B. *et al.* MolProbity: all-atom structure validation for macromolecular
354 crystallography. *Acta Crystallogr. D Biol. Crystallogr.* **66**, 12–21 (2010).

355 37 Afonine, P. V. *et al.* FEM: feature-enhanced map. *Acta Crystallogr. D Biol. Crystallogr.*
356 **71**, 646-666 (2015).
357 38 Whittington, D. A. & Lippard, S. J. Crystal structures of the soluble methane
358 monooxygenase hydroxylase from Methylococcus capsulatus (Bath) demonstrating
359 geometrical variability at the dinuclear iron active site. *J. Am. Chem. Soc.* **123**, 827–838
360 (2001).
361 39 Whittington, D. A., Sazinsky, M. H. & Lippard, S. J. X-ray crystal structure of alcohol
362 products bound at the active site of soluble methane monooxygenase hydroxylase. *J. Am.*
363 *Chem. Soc.* **123**, 1794–1795 (2001).
364 40 Petrek, M. *et al.* CAVER: a new tool to explore routes from protein clefts, pockets and
365 cavities. *BMC Bioinformatics* **7**, 316 (2006).
366

367 **Acknowledgments**

368 We thank the staff at the Advanced Photon Source LS-CAT beamline for their advice and
369 assistance with data collection. We thank Dr Stephen Ragsdale, Dr Youngmin You and Dr David
370 Ballou for helpful discussions and comments on the manuscript. This work was supported in part
371 by grants (the C1 Gas Refinery Program through the National Research Foundation of Korea
372 [NRF-2015M3D3A1A01064876]) to S.J.L., and by grants (The Biomedical Research Council
373 [BMRC] bridging fund [University of Michigan] and R01 DK111465) to U.S.C.

374 **Author Contributions**

375 H.K. obtained the crystals, solved, and refined the structures, analysed data and wrote the
376 manuscript; S.A. purified proteins, analysed data and wrote the manuscript; Y.R.P. cultured *M.*
377 *sporium* 5 and purified proteins for catalytic activity and affinity measurements; H.J. expressed
378 and purified truncated MMOD; S.H.P. assisted structural determination; S.J.L. designed
379 experiments for catalytic activity and binding measurement, analysed data and wrote the
380 manuscript; and U.S.C. directed the project, designed experiments, analysed data and wrote the
381 manuscript. All authors discussed the results and commented on the manuscript.

382

383 **Author Information**

384 **Data availability.** Coordinates and structure factors for the reported crystal structure of the *M.*
385 *sporium* strain 5 MMOH–MMOD complex have been deposited with the Protein Data Bank
386 under accession code 6D7K.

387 **Competing interests.** The authors declare no competing interests.

388 *Corresponding Authors: Email: uhnsoo@med.umich.edu; Tel.: 1-(734)764-6765; Fax: 1-
389 (734)763-4581. E-mail: slee026@jbnu.ac.kr; Tel.: 82-(63)270-3412; Fax: 82-(63)270-3408

390

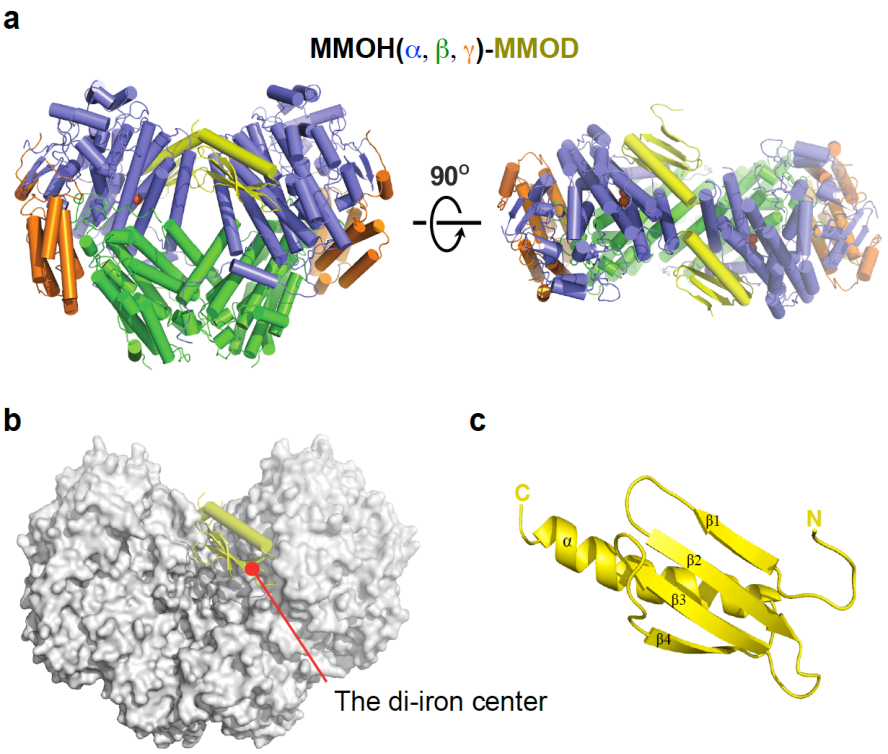

391

392 **Figure 1 | Crystal structure of the MMOH–MMOD complex. a**, Front and top views of the
393 MMOH–MMOD complex. MMOH is shown using a cartoon model (α-subunit: blue, β-subunit:
394 green γ-subunit: orange); MMOD is coloured yellow. **b**, Front view of the MMOH–MMOD
395 complex. MMOH is shown using a surface representation model (white) and MMOD (yellow) is
396 shown in cartoon form. Red circle marks the location of the di-iron centre in MMOH. **c**, MMOD
397 contains a ββββα-fold, which is shown in cartoon form. Illustrations of the protein structure used
398 in all figures were generated with PyMOL (Delano Scientific, LLC).

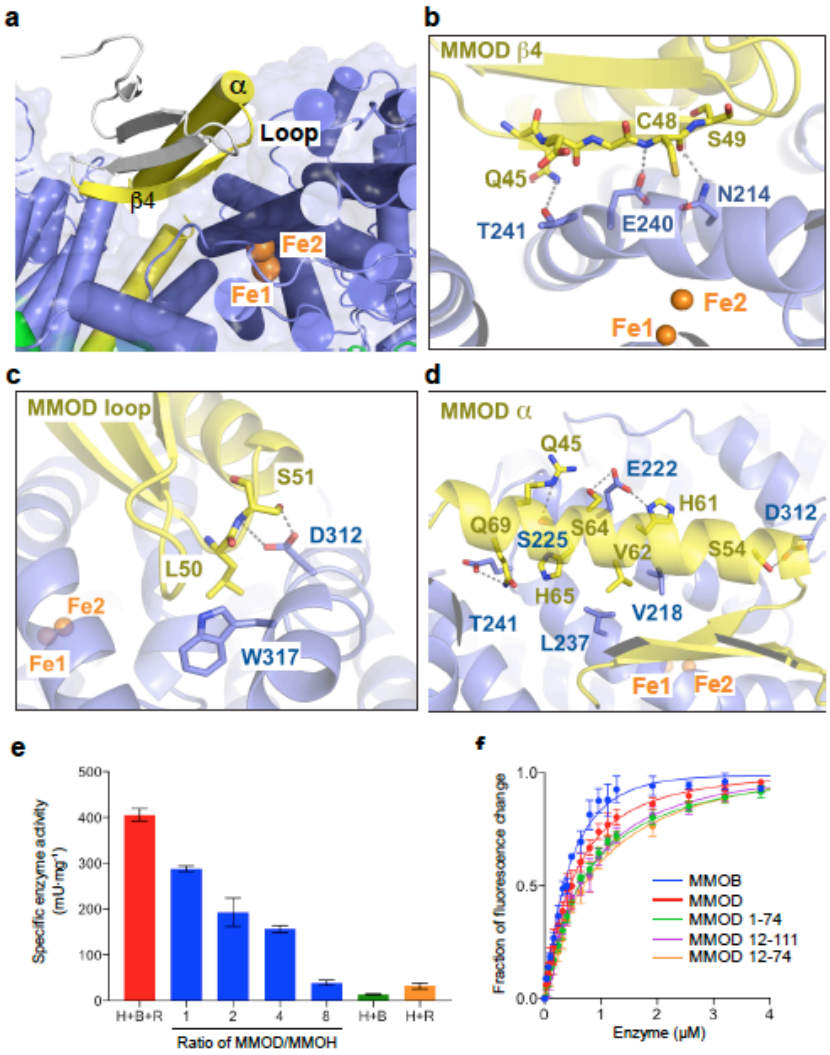

Figure 2 | Key residues participate in both the MMOH–MMOD binding and the inhibitory activity of MMOD. a, MMOD β4, loop and helix α (yellow) directly participate in recognising the canyon region of MMOH. MMOD residues that do not interact with MMOH are coloured grey. The two iron atoms are labelled and coloured orange. **b–d**, Detailed interactions in the MMOH–MMOD complex. **e**, Enzymatic activities (n = 3) of MMOH in the presence of MMOB, MMOR and/or MMOD, as determined based on the conversion from propylene to propylene oxide in the presence of NADH. Condition H+B+R (red) indicates the absence of MMOD; blue indicates the addition of MMOD. Conditions H+B (green) and H+R (orange) represent the

408 absence of MMOR and MMOB, respectively (n = 3, Ave ± SEM). **f**, Binding of MMOB,
409 MMOD and truncated MMODs to MMOH as detected by fluorescence spectroscopy (n = 3). All
410 error bars represent SEMs. Quenching of intrinsic fluorescence of MMOH was monitored by
411 titration of the MMOB (blue), MMOD (red), 1–74 MMOD (green), 12–111 MMOD (purple),
412 and 12–111 MMOD (orange). The K_{D1} and K_{D2} values were determined through nonlinear curve
413 fitting for two binding sites of MMOH (0.32 μM).

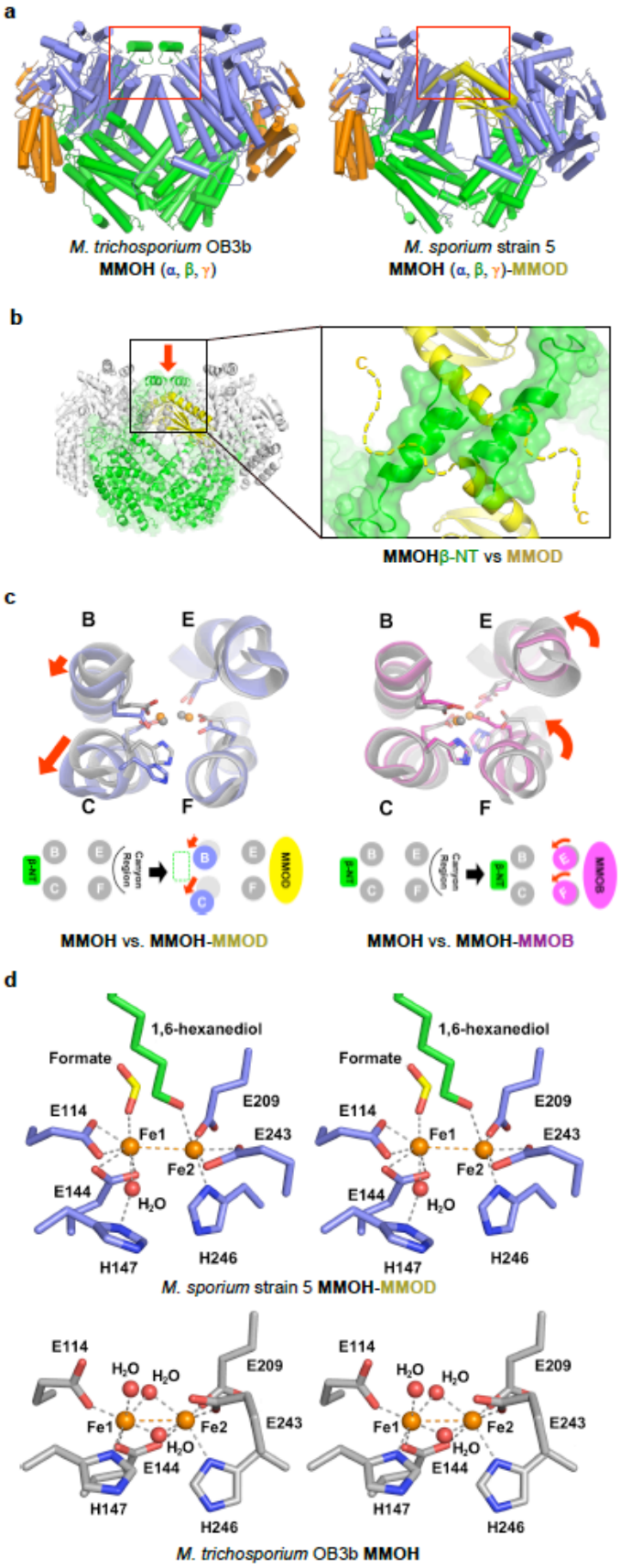
a
M. trichosporium OB3b
MMOH (α, β, γ)
M. sporium strain 5
MMOH (α, β, γ)-MMOD
b
C
C
MMOHβ-NT vs MMOD
c
B
E
C
F
B
E
C
F
MMOH vs. MMOH-MMOD
MMOH vs. MMOH-MMOB
d
1,6-hexanediol
Formate
E114
E209
Fe1
E243
Fe2
E144
H2O
H147
H246
M. sporium strain 5 MMOH-MMOD
M. trichosporium OB3b MMOH

414

415 **Figure 3 | Structural comparison of MMOH (PDB ID: 1MHY)[20] and MMOH–MMOD. a**,
416 Front views of MMOH and MMOH–MMOD. Red box indicates the region with the major
417 structural differences. **b**, *M. sporium* strain 5 MMOD structures are overlaid onto *M.*
418 *trichosporium* OB3b MMOH. N-terminus of MMOH β-subunit is displayed in green. MMOD C-
419 terminal long helix is shown in yellow. Dashed yellow lines indicate the extended, disordered C-
420 terminal region of MMOD. The red arrow indicates the viewing angle of inset. The inset shows
421 the clash between MMOHβ-NT and the C-terminal helix of MMOD. **c**, Conformational changes
422 in the MMOH four-helix bundle (helices B, C, E and F) upon MMOB and MMOD binding. Six
423 residues that coordinate two iron atoms are on helices B, C, E and F. Red arrows indicate the
424 translation and rotation of indicated helices upon MMOD and MMOB binding. **d**, Stereo-views
425 of the di-iron centre geometry in MMOH–MMOD and MMOH. Two Fe atoms (orange) are
426 surrounded and coordinated by four glutamate and two histidine residues. Water molecules
427 (H_2O) are displayed as red spheres.

428

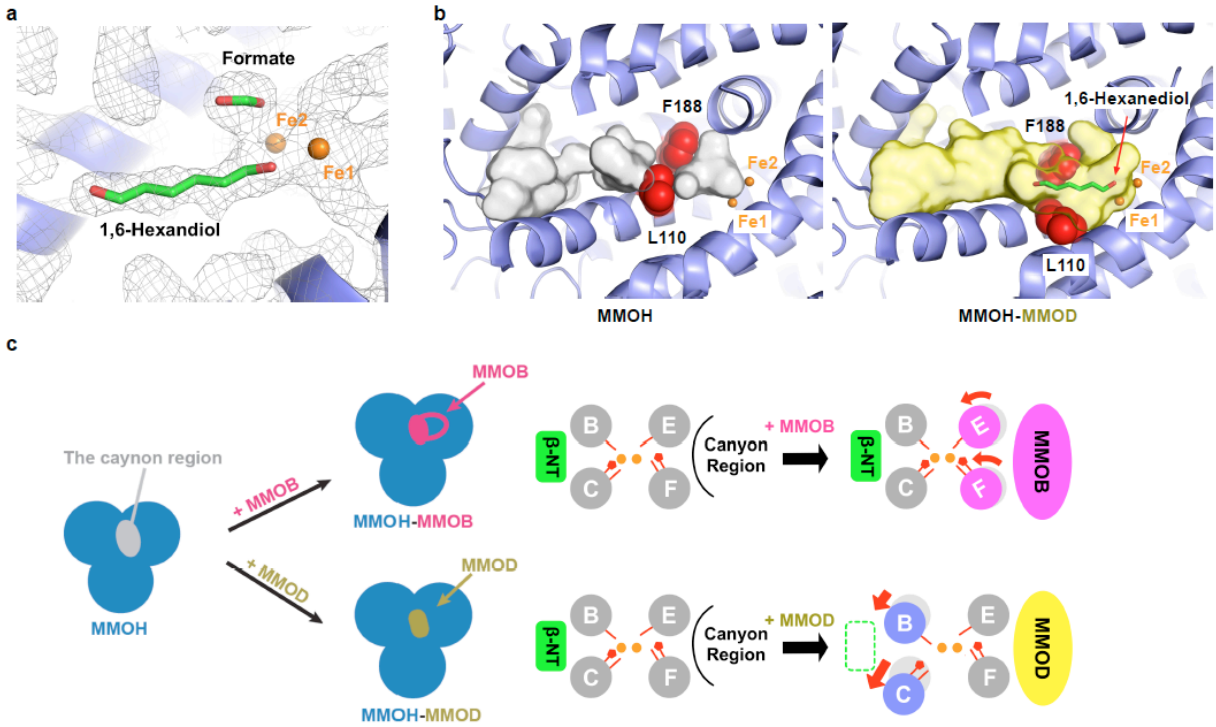

429

430 **Figure 4 | A product analogue (1,6-hexanediol) at the substrate access channel near the di-**

431 **iron centre and the channel opening in the MMOH–MMOD complex. a**, The composite omit

432 map (1.5-σ contour, calculated using the PHENIX software package[37]) of MMOH–MMOD near

433 the di-iron centre. The electron density map is shown as mesh (grey), and 1,6-hexanediol and

434 formate are coloured green. **b**, The substrate access channel in the *M. trichosporium* OB3b

435 MMOH (grey, PDB ID: 1MHY)[20] and the *M. sporium* strain 5 MMOH-MMOD complex

436 (yellow). Two gate forming residues (Leu110 and Phe188) are shown as red spheres and 1,6-

437 hexandiol is shown in green. The channels calculated using PyMOL are shown as surface

438 models. **c**, A schematic model showing the association of MMOH with its auxiliary proteins–

439 MMOB and MMOD, which compete for the canyon region of MMOH.

440

441 **Extended Data Table 1 | Data collection and refinement statistics**

442

	M. sporium strain 5 MMOH–MMOD Complex*
Data collection	
Space group	C 1 2 1
Cell dimensions	
a, b, c (Å)	179.78, 125.78, 126.38
α, β, γ (°)	90.00, 102.89, 90.00
Resolution (Å)	50.00–2.60 (2.64-2.60) **
R_{sym} or R_{merge}	12.4 (79.3)
I / σI	12.8 (1.6)
Completeness (%)	99.5 (98.9)
Redundancy	4.3 (4.2)
Number of reflections	362,653
Unique	84,164
Refinement	
Resolution (Å)	22.29–2.60 (2.66–2.60)
No. reflections	83,613
R_{work} / R_{free}	0.179 / 0.220
No. of atoms	
Protein	17,401
Ligand/ion	28
Water	339
B-factors	
Protein	48.71
Ligand/ion	38.88
Water	42.40
R.M.S. deviations	
Bond lengths (Å)	0.008
Bond angles (°)	0.891

443 *PDB ID 6D7K **Values in parentheses are for highest-resolution shell

444

445 **Extended Data Table 2 | Dissociation constants for binding of MMOH with MMOB,**

446 **MMOD, and truncated MMODs**

$$\mathrm{MMOH} + \mathrm{E} \underset{}{\overset{K_{D1}}{\rightleftharpoons}} \mathrm{MMOH} \cdot \mathrm{E} \overset{K_{D2}}{\rightleftharpoons} \mathrm{MMOH} \cdot \mathrm{E}_2 \quad (1)$$

447

448

Enzymes	K_{D1} (μM)	K_{D2} (μM)
MMOB	0.04 ± 0.01	0.86 ± 0.16
MMOD	0.59 ± 0.03	0.90 ± 0.14
MMOD (1–74)	0.82 ± 0.10	2.69 ± 0.28
MMOD (12–111)	0.93 ± 0.06	2.75 ± 0.26
MMOD (12–74)	1.14 ± 0.10	2.90 ± 0.61

449

450 The intensities of intrinsic fluorescence of MMOH were partially quenched by titration of
451 enzymes, and two binding sites of MMOH were used with nonlinear curve fitting (equation 1, n
452 = 3, Ave ± SEM). E represents MMOB, MMOD, and truncated MMOD (1–74, 12–111 and 12–
453 74).

a

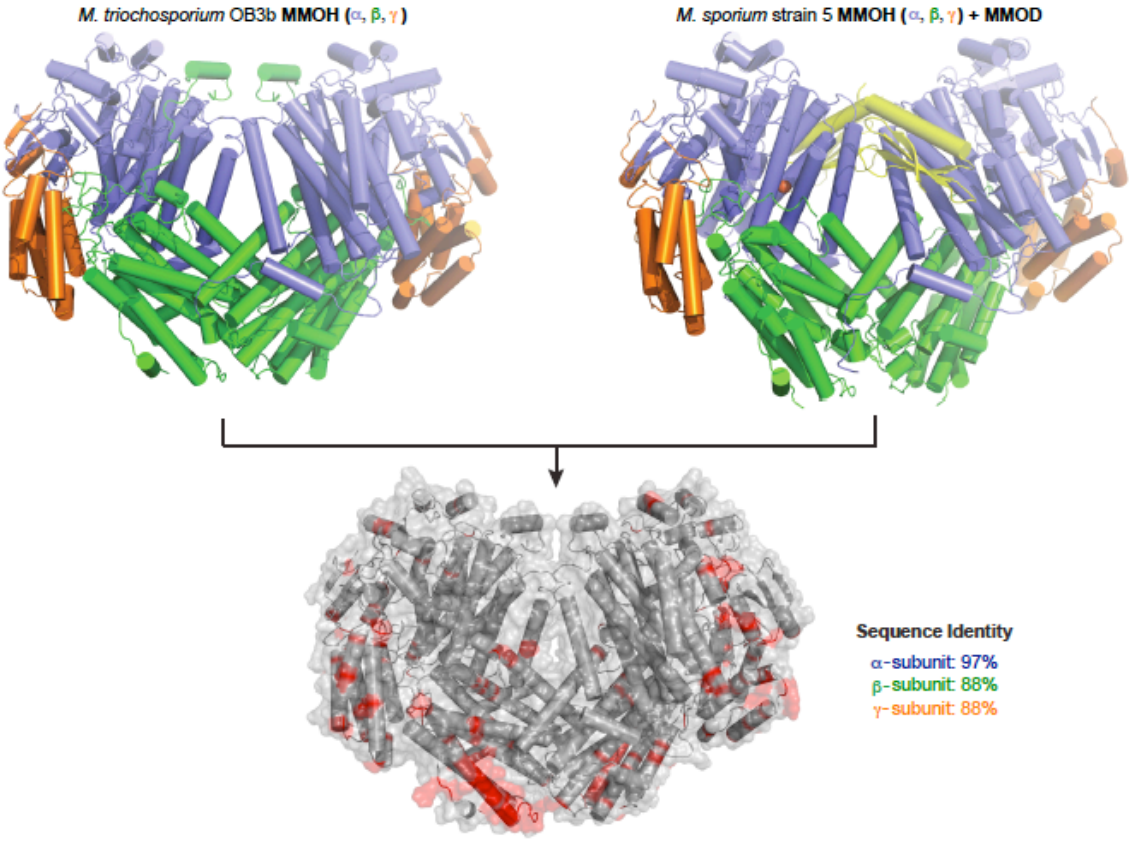

b

α-subunit

```
M. sporium strain5     MAISLATKAATDALKVNRAPVGVEPQEVHKWLQSFNWDFKENRTKYATKYHMANQTKEQF 60
M. trichosporium OB3b  MAISLATKAATDALKVNRAPVGVEPQEVHKWLQSFNWDFKENRTKYPTKYHMANETKEQF 60
                       ********************************************** *******:******

M. sporium strain5     KVIAKEYARMEAAKDERQFGTLLDGLTRLGAGNKVHPRWGETMKVISNFLEVGEYNAIAA 120
M. trichosporium OB3b  KVIAKEYARMEAAKDERQFGTLLDGLTRLGAGNKVHPRWGETMKVISNFLEVGEYNAIAA 120
                       ************************************************************

M. sporium strain5     SAMLWDSATAAEQKNGYLAQVLDEIRHTHQCAFINHYYSKHYHDPAGHNDARRTRAIGPL 180
M. trichosporium OB3b  SAMLWDSATAAEQKNGYLAQVLDEIRHTHQCAFINHYYSKHYHDPAGHNDARRTRAIGPL 180
                       ************************************************************

M. sporium strain5     WKGMKRVFADGFISGDAVECSVNLQLVGEACFTNPLIVAVTEWASANGDEITPTVFLSVE 240
M. trichosporium OB3b  WKGMKRVFADGFISGDAVECSVNLQLVGEACFTNPLIVAVTEWASANGDEITPTVFLSVE 240
                       ************************************************************

M. sporium strain5     TDELRHMANGYQTVVSIANDPAAAKYLNTDLNNAFWTQQKYFTPALGYLFEYGSKFKVEP 300
M. trichosporium OB3b  TDELRHMANGYQTVVSIANDPASAKFLNTDLNNAFWTQQKYFTPVLGYLFEYGSKFKVEP 300
                       **********************:**:******************.***************

M. sporium strain5     WVKTWNRWVYEDWGGIWIGRLGKYGVESPRSLRDAKTDAYWAHHDLALAAYALWPLGFAR 360
M. trichosporium OB3b  WVKTWNRWVYEDWGGIWIGRLGKYGVESPASLRDAKRDAYWAHHDLALAAYAMWPLGFAR 360
                       **************************** ****** ***************:*******

M. sporium strain5     LALPDEEDQEWFEANYPGWADHYGKIYNEWKKLGYEDPKSGFIPYAWLLANGHDVYIDRV 420
M. trichosporium OB3b  LALPDEEDQAWFEANYPGWADHYGKIFNEWKKLGYEDPKSGFIPYQWLLANGHDVYIDRV 420
                       ********* ***************:****************** **************

M. sporium strain5     SQVPFIPSLAKGSGSLRVHEFNGKKHSLTDDWGERMWLSEPERYECHNLFEQYEGRELSE 480
M. trichosporium OB3b  SQVPFIPSLAKGTGSLRVHEFNGKKHSLTDDWGERQWLIEPERYECHNVFEQYEGRELSE 480
                       ************:********************** ** *********:************

M. sporium strain5     VIAEGHGVRSDGKTLIAQPHVRGDNLWTLEDIKRAGCVFPNPLAKF 526
M. trichosporium OB3b  VIAEGHGVRSDGKTLIAQPHTRGDNLWTLEDIKRAGCVFPDPLAKF 526
                       ********************.*******************:*****
```

454

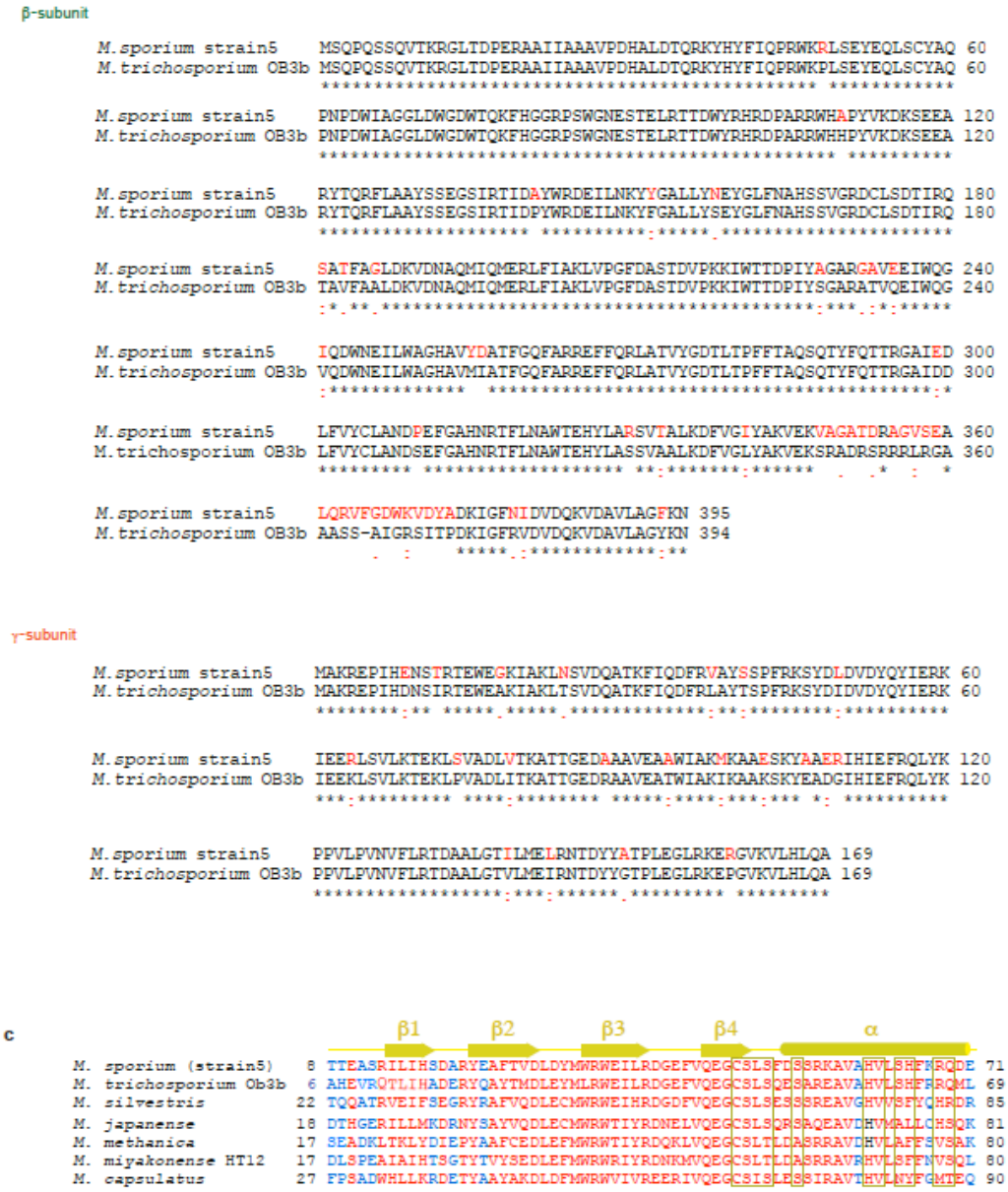

455

456 **Extended Data Figure 1 | Primary sequence conservation of *M. trichosporium* OB3b and *M.***
457 ***sporium* strain 5 MMOHs and multiple sequence alignment of MMOD. a**, Structure
458 comparison of *M. trichosporium* OB3b MMOH and *M. sporium* strain 5 MMOH–MMOD. The
459 primary sequence identities of α-, β- and γ-subunits in *M. trichosporium* OB3b and the *M.*
460 *sporium* strain 5 MMOHs are 97%, 88% and 88%, respectively. Residues that differ in *M.*

461 *trichosporium* OB3b and the *M. sporium* strain 5 MMOHs are coloured red. Residues involved
462 in MMOD recognition and di-iron centre formation are 100% conserved in *M. trichosporium*
463 OB3b and the *M. sporium* strain 5 MMOHs. **b**, The primary sequence comparison of α-, β- and
464 γ-subunits in *M. trichosporium* OB3b and the *M. sporium* strain 5 MMOHs. MMOH residues
465 that differ in *M. trichosporium* OB3b and the *M. sporium* strain 5 are coloured red. **c**, The
466 multiple sequence alignment of the MMOD core region (residues 8–71 in *M. sporium* strain 5
467 MMOD) among methanotrophs. Residues that have high sequence similarity are coloured red;
468 others are coloured blue. Residues that participate in the MMOH interactions are boxed in
469 yellow. Corresponding secondary structures of MMOD are indicated above the sequence
470 alignment.

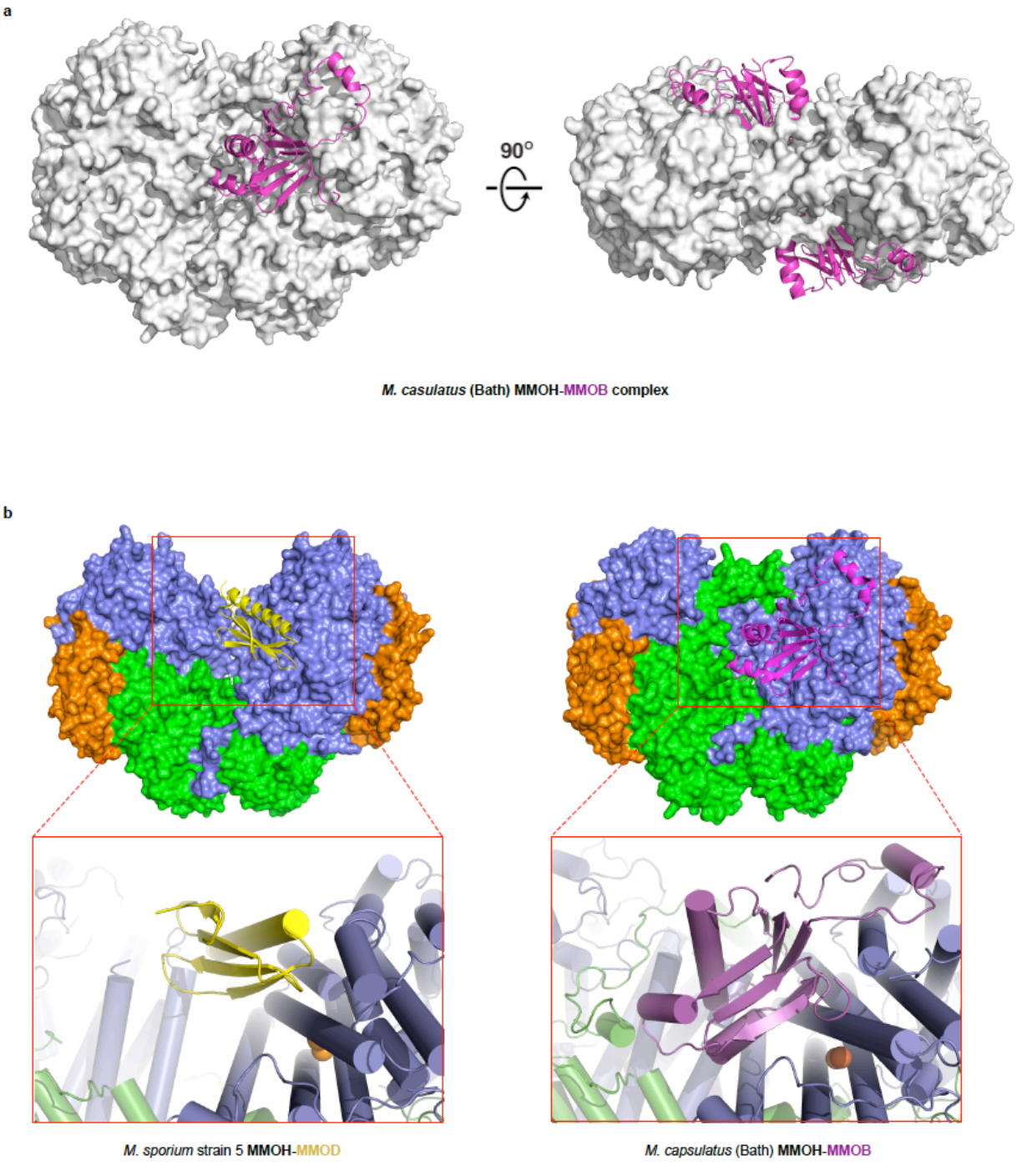

471

472 **Extended Data Figure 2 | Crystal structure of the *M. capulatus* MMOH–MMOB complex**
473 **(PDB ID: 4GAM)**[15] **and the structural comparison of MMOD (*M. sporium* strain 5) and**
474 **MMOB (*M. capsulatus*) binding to MMOH. a**, front and top views of the *M. capsulatus*

475 MMOH–MMOB complex. MMOH is shown using surface representation model (white) and
476 MMOB (purple) is shown using a cartoon model. **b**, The structural comparison of MMOH–
477 MMOD (*M. sporium* strain 5) and MMOH–MMOB (*M. capsulatus*) complexes. Areas with the
478 red box are magnified to visualise the binding patterns of MMOD (yellow) and MMOB (purple)
479 at the canyon region of MMOH. Although the overall architectures of MMOD and MMOB are
480 quite distinct, both MMOD and MMOB bind competitively at the same canyon region of
481 MMOH.

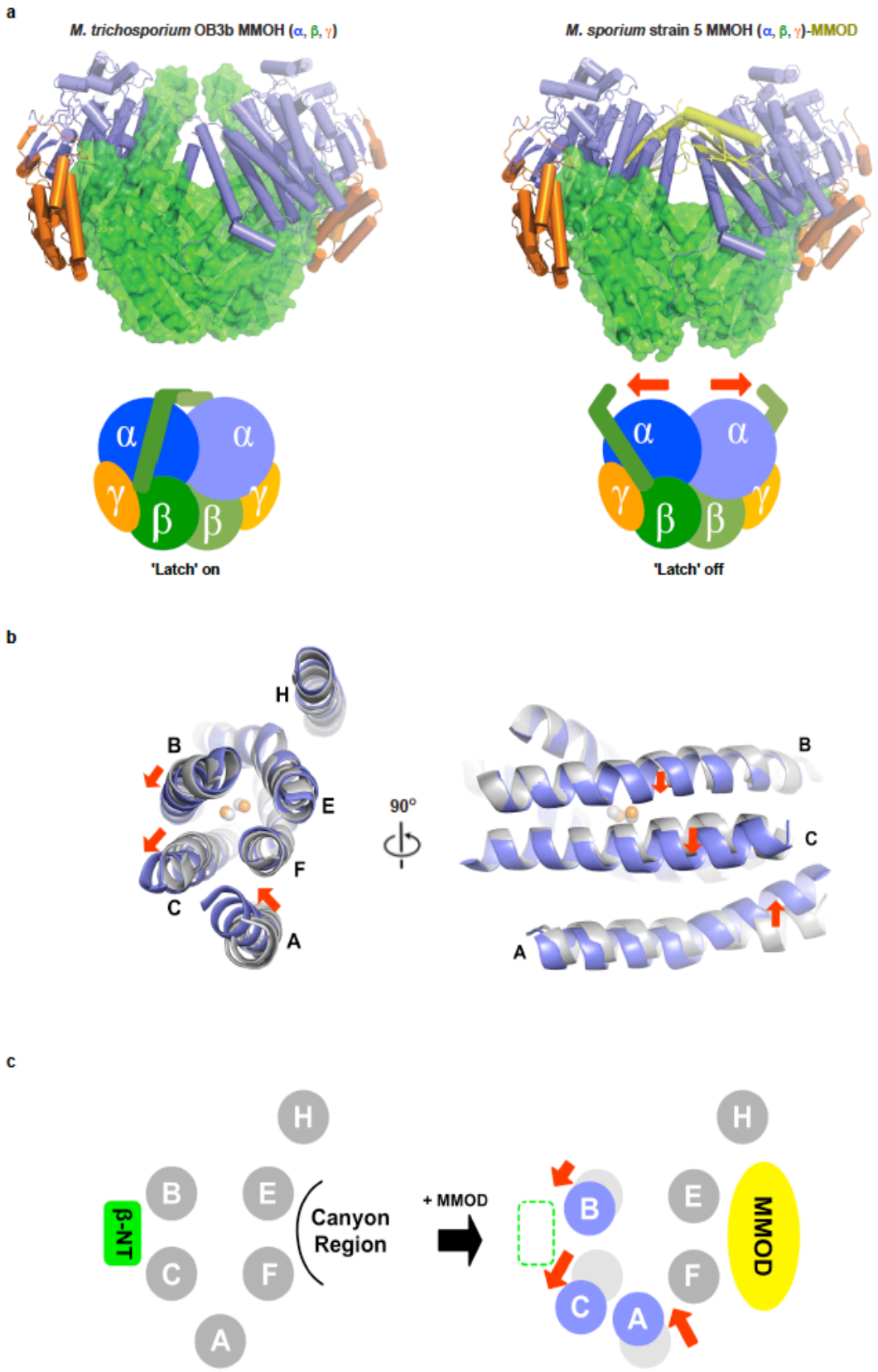
a
M. trichosporium OB3b MMOH (α, β, γ)
M. sporium strain 5 MMOH (α, β, γ)-MMOD
α
α
γ
β
β
γ
'Latch' on
'Latch' off
b
H
B
E
F
C
A
90°
c
β-NT
Canyon Region
+ MMOD
MMOD

482

483 **Extended Data Figure 3 | Conformational changes in MMOH upon MMOD binding. a**,
484 Structural comparison of MMOH (*M. trichosporium* OB3b) and the MMOH–MMOD complex
485 (*M. sporium* strain 5). MMOHβ is shown using the surface representation model and other
486 subunits (α and γ), including MMOD, are shown as cartoon models. Structural comparison
487 indicates that the N-terminal region of MMOHβ (β-NT) is disordered upon MMOD association.
488 The schematic model shows that MMOHβ-NT may function as a 'latch' to tightly lock MMOHα
489 helix bundles. MMOD binding unlocks the 'latch' and relaxes the overall helix architecture of
490 MMOHα, as shown in **b** and **c**. **b**, Top and side views of MMOHα helices (A, B, C, E, F and H)
491 before (grey, PDB ID: 1MHY)[20] and after (blue) MMOD association. MMOD binding breaks the
492 interaction between MMOHβ-NT ('latch off') of two protomers and thus induces conformational
493 relaxation of MMOHα, including helices A, B, and C. Red arrows indicate the direction of helix
494 movement after MMOD association and the MMOHβ-NT latch off. Two iron atoms are shown
495 using the sphere model (before: grey, after: orange)**.** **c**, Schematic representation of MMOHα
496 helix movement upon MMOD association. MMOD binding causes MMOHβ-NT to 'latch off',
497 which then leads to the movement of helices A, B and C owing to the loss of support from
498 MMOHβ-NT.

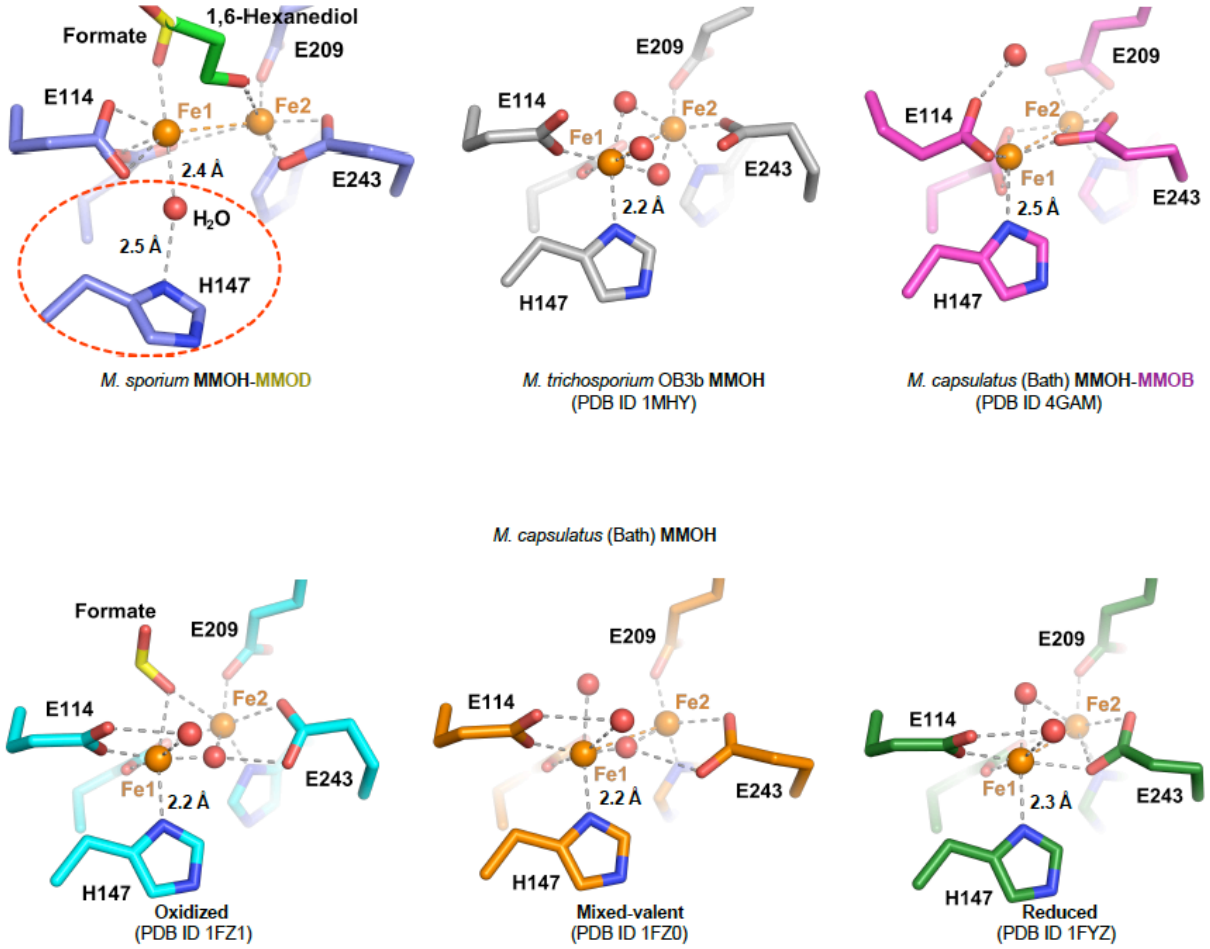

Extended Data Figure 4 | Geometry of the di-iron active site in the MMOH–MMOD complex and its structural comparison with other known MMOH structures. The geometry of the di-iron centre in the MMOH–MMOD complex differs significantly from other known MMOH di-iron centre geometries. There is dissociation of His147 from Fe1 coordination (red dotted circle) as well as bidentate recognition of Glu114 towards Fe1. A water molecule bridges the Fe1 coordination of His147. Distances between Fe1 and Nδ1 atom of His147 are indicated in each structure.

a

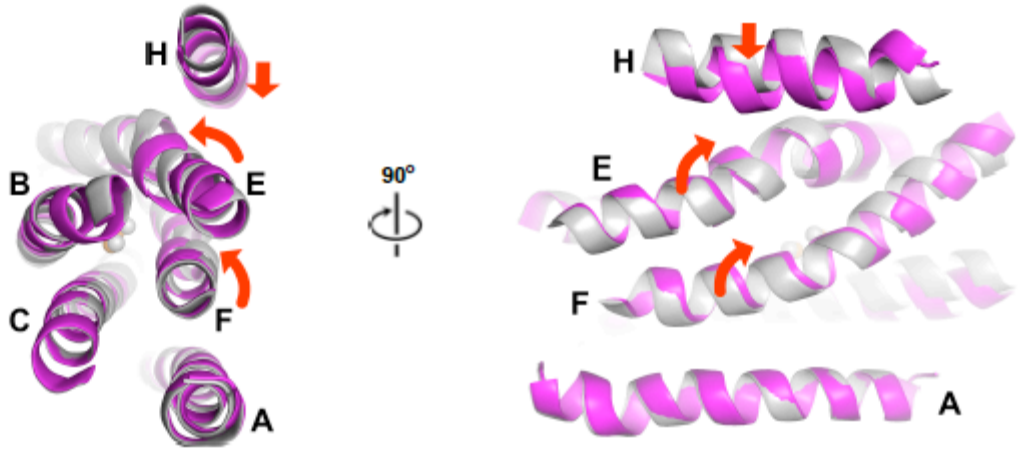
H
B
E
C
F
A
90°
H
E
F
A

b

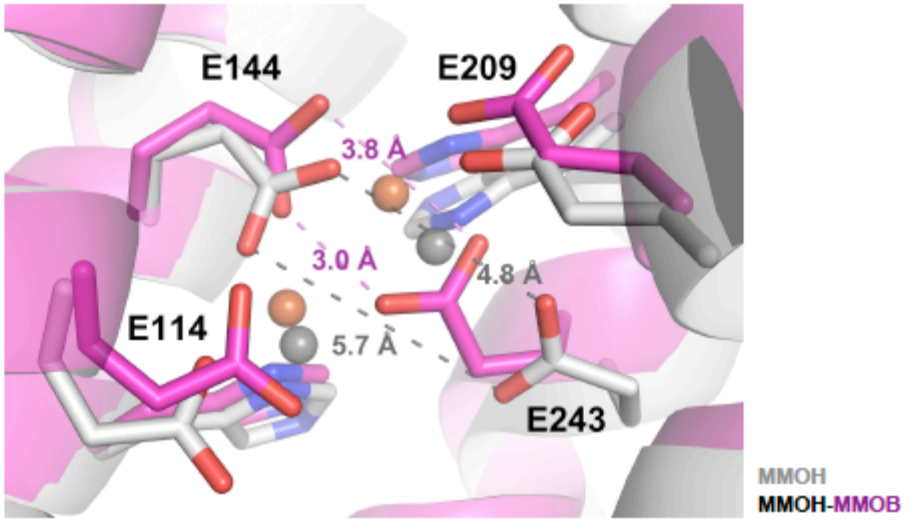
E144
E209
3.8 Å
3.0 Å
4.8 Å
E114
5.7 Å
E243
MMOH
MMOH-MMOB

c

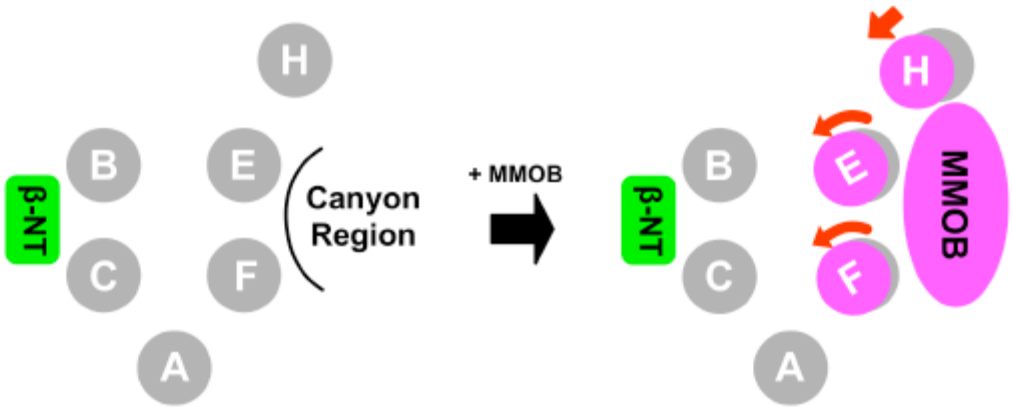
H
B
E
β-NT
C
F
A
Canyon
Region
+ MMOB
H
B
E
β-NT
C
F
A
MMOB

508

509 **Extended Data Figure 5 | The movement of helices in MMOHα upon MMOB binding. a**,
510 Top and side-views of MMOHα helices (A, B, C, E, F and H) before (grey, PDB ID: 1FZ1)[38]
511 and after (purple, PDB ID: 4GAM)[15] MMOB association in the *M. capsulatus* (Bath) MMOH–
512 MMOB complex. MMOB binding causes the movement of helix H and the counter-clockwise
513 rotation of helices E and F in MMOHα. **b**, Geometry changes in the di-iron centre upon MMOB
514 association. MMOB binding induces the rotation of helices E and F, which contain iron
515 coordinating Glu209 (helix E) as well as Glu243 and His246 (helix F). Particularly, rotation of
516 helix F forces Glu243 to get close to the di-iron centre, thereby decreasing the distance between
517 Glu144 and Glu243 (oxygen–oxygen distances decrease from 5.7 Å and 4.8 Å to 3.0 ± 0.2 Å and
518 3.8 ± 0.2 Å). Consequently, two irons become tightly coordinated by Glu144 and Glu243,
519 causing changes in the reduction potential. **c**, The schematic representation of MMOHα helix
520 movement upon MMOB association. MMOB binding causes the rotations of MMOHα helices E
521 and F, which induce the rearrangement of the geometry of the di-iron centre.

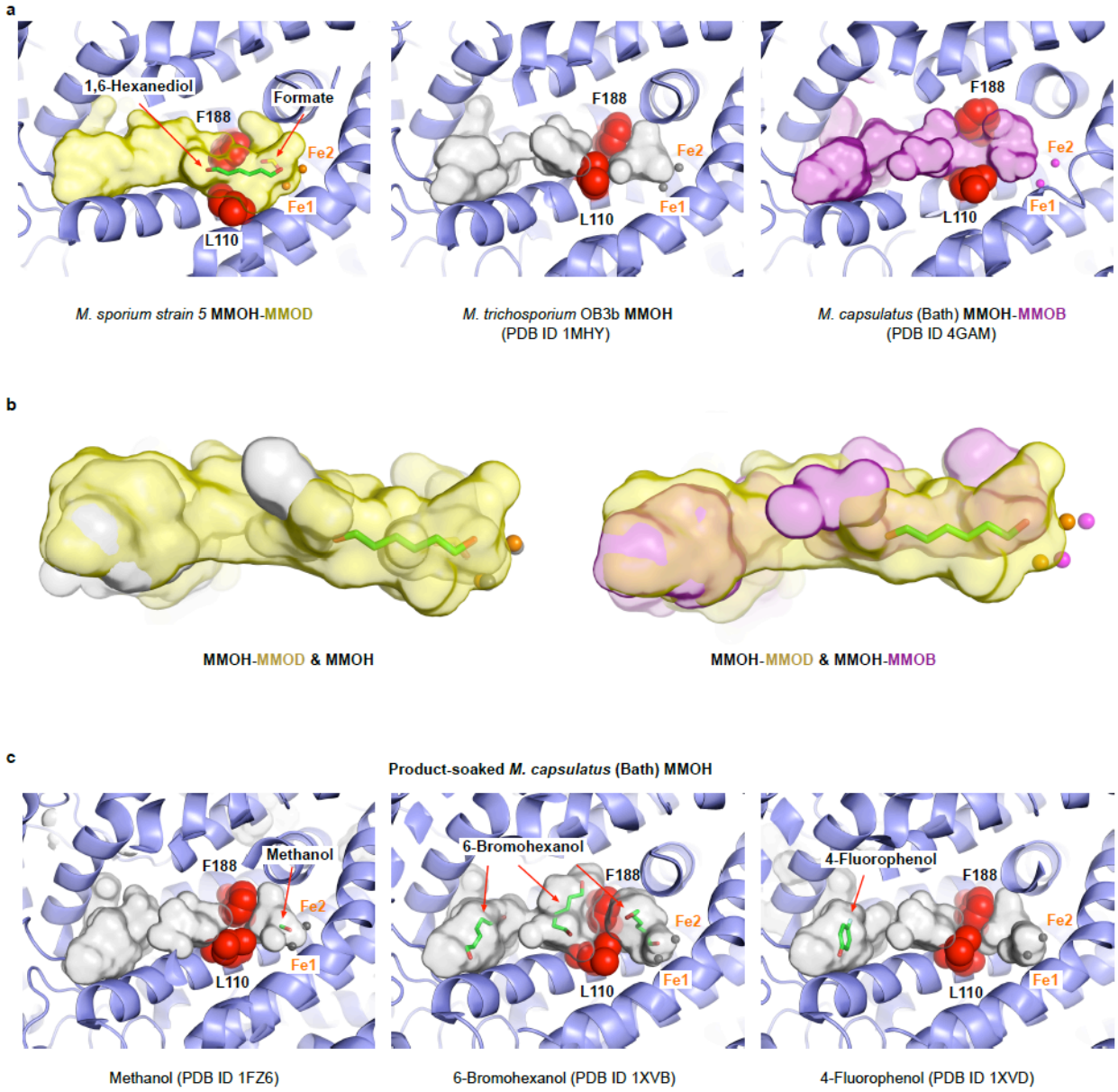

Extended Data Figure 6 | Comparison of the substrate access channel in MMOH (PDB ID: 1MHY)[20], MMOH–MMOB (PDB ID: 4GAM)[15] and MMOH–MMOD. a, Cavities of the substrate access channel in MMOH (grey), MMOH–MMOB (purple) and MMOH–MMOD (yellow) are displayed as surface representation models. The gate forming residues (Leu110 and Phe188) are shown as spheres of red colour. A product analogue, 1,6-hexanediol, is also shown using stick representation (green). In MMOH, the substrate access channel to the di-iron centre is

529 disconnected by gate-forming residues. In both MMOH–MMOB and MMOH–MMOD, the gate
530 is open. **b**, Comparison of the substrate access channel in MMOH–MMOD and MMOH, as well
531 as MMOH–MMOD and MMOH–MMOB. In both cases, the substrate access channel in the
532 MMOH-MMOD complex is wider, probably owing to the overall structural relaxation of
533 MMOHα caused by MMOHβ-NT disorganisation. **c**, The substrate access channel in *M.*
534 *capsulatus* (Bath) MMOH soaked with various products or product analogues. Substrate access
535 channels in the presence of methanol (PDB ID: 1FZ6)[39], 6-bromohexanol (PDB ID: 1XVB)[26],
536 and 4-florophenol (PDB ID: 1XVD)[26] are displayed as surface representation models. In all
537 cases, gate closure is mediated by Leu110 and Phe188, and products (substrate analogues) are
538 trapped in either one or all of the three cavities. All channels are shown as surface models, which
539 were calculated using PyMOL.

540

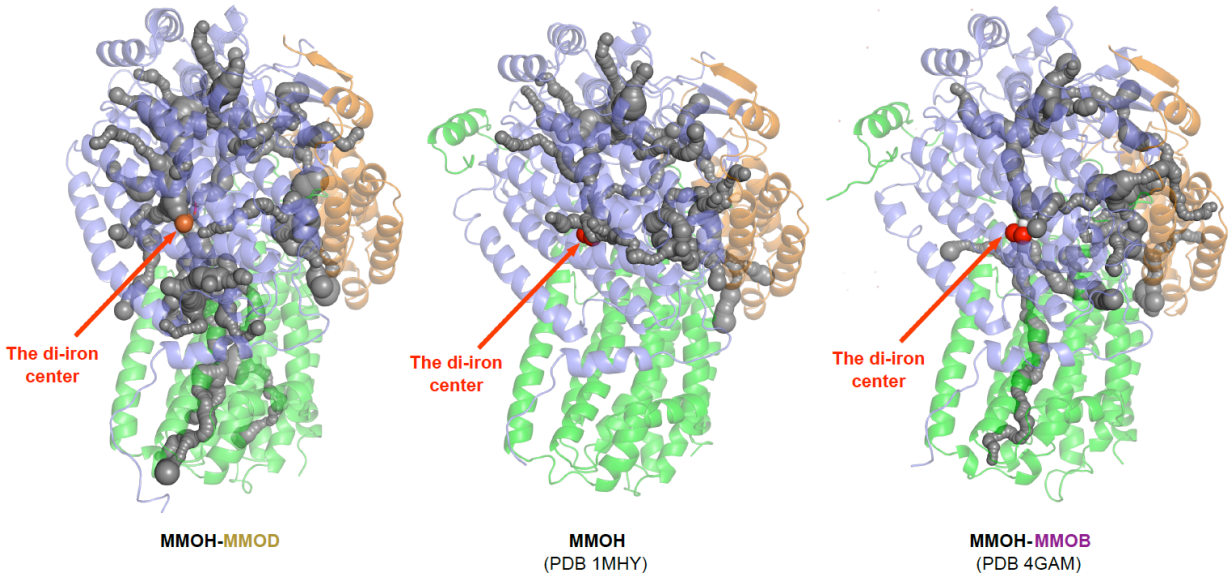

Extended Data Figure 7 | Comparisons of internal cavities within the MMOH protomer of MMOH–MMOD, MMOH and MMOH–MMOB. The MMOH protomer is presented in cartoon form; α-subunit (blue), β-subunit (green) and γ-subunit (orange). The di-iron centre is shown as orange (MMOH–MMOD) and red spheres (MMOH and MMOH–MMOB). Internal cavities calculated using CAVER[40] are shown as chains of grey spheres. The CAVER analysis of MMOH protomers reveals that MMOD association produces more internal cavities when compared to MMOH alone and MMOH–MMOB. CAVER 3.0 (PyMOL plug-in) with the default setting was used to calculate internal cavities.